

## Dynamical Jahn-Teller and reorientation effects in the EPR spectrum of $\text{CaF}_2:\text{O}^{\cdot-}$

Hans Bill

*University of Geneva, Geneva, Switzerland*

R. H. Silsbee

*Cornell University, Ithaca, New York*

(Received 7 May 1974)

The  $\text{O}^{\cdot-}$  ion, substitutional for  $\text{F}^-$  in  $\text{CaF}_2$ , shows a Jahn-Teller effect associated with the electronic degeneracy of the unfilled  $p$  shell. The different Jahn-Teller distortions are coupled to each other via a partially quenched spin-orbit energy. The magnitude of this coupling,  $\sim 0.15 \text{ cm}^{-1}$ , may be estimated from an interpretation of the effects of applied stress on the low-temperature EPR spectrum. This coupling also results in reorientation of the center via a phonon-assisted tunneling process, whose magnitude can be estimated experimentally from the thermal broadening of the EPR in the range (5–20) °K, and theoretically, without adjustable parameters, from the results of the low-temperature experiments and the elastic constants of the host crystal. The results are in reasonable accord, giving support both to the proposed model for the center and to the usual theory for the phonon-assisted tunneling rates.

### I. INTRODUCTION

Recent treatments of Jahn-Teller (JT) systems in crystals (see, e.g., Sturge<sup>1</sup> and Ham<sup>2</sup> for very comprehensive and complete reviews) consider, and emphasize, the important consequences resulting from the inclusion of the lattice movement. Usually this motion is included by considering the Jahn-Teller ion together with the coordination neighbors as an independent molecule oscillating in one or several of its normal modes. This approach although simplifying the real problems has been very successful in interpreting several recent Jahn-Teller systems. Most of these involve  $E$ -type electronic ground states (e.g.,  $\text{Cu}^{2+}$ ,  $^3R$  center,  $^4\text{Pt}^{3+}$ ,  $^5\text{Sc}^{2+}$ ,  $^6\text{La}^{2+}$ ,  $^7$  etc), and exhibit dynamical features in their EPR spectra. This is due to the fact that orientational localization of the center is not a result of the linear JT effect but either of a supplementary crystal field of lower than cubic symmetry or of suitable anharmonic terms in the elastic potential which are usually much smaller than the linear JT term. In addition, there are a few triplet ground-state systems, which have been at the origin of the general understanding of the dynamical Jahn-Teller effect (Ham<sup>8</sup>), namely,  $\text{Fe}^{2+}$ ,  $\text{Mn}^+$ , and  $\text{Cr}^0$  in Si.<sup>9</sup> All of these exhibit a purely dynamical effect.

The present paper reports an experimental investigation of the paramagnetic  $\text{O}^{\cdot-}$  ion in  $\text{CaF}_2$  and to some extent also in  $\text{SrF}_2$ . The  $p$ -symmetry electronic ground state involved transforms as a  $T_1$  triplet and couples predominantly to lattice modes of  $E$  symmetry. The observed Jahn-Teller effect is essentially static. However, the system relaxes among the different distorted configurations. The hopping frequency is high enough even

at low temperatures to play a very important part in the relaxation behavior of the system. By investigating the EPR linewidth and the saturation behavior as a function of temperature, semiquantitative estimates of the tunneling matrix element have been made and the reorientation time determined.

It is useful at this point to mention some evidence showing the importance of the motional effects on the relaxation behavior of the center by comparing it with  $(\text{OF})^{2-}$  in  $\text{CaF}_2$ .<sup>10</sup> This latter center is similar to the one discussed here, except that there is a fluorine vacancy associated with the  $\text{O}^{\cdot-}$  ion in the  $(\text{OF})^{2-}$  center. It possesses EPR parameters comparable to the  $\text{O}^{\cdot-}$  centers (see Table I). However, as the symmetry of the  $(\text{OF})^{2-}$  is sufficiently low, due to the associated vacancy, no Jahn-Teller effect is involved in this case. The center is observed at temperatures  $\leq 110$  °K. No line-broadening effects show up below this temperature ( $\Delta B_{pp} \approx 8$  G). In fact, the center saturates heavily at 4.2 °K with about  $10^{-3}$  G ( $H_1$ ) rf field. The  $\text{O}^{\cdot-}$  center, instead, is not observed at 78 °K and at 4 °K is just beginning to saturate with  $H_1 \approx 1$  G. This striking difference in the relaxation behavior of the centers arises from the Jahn-Teller effect being present and involving dynamical features in the case of the  $\text{O}^{\cdot-}$  center and being absent in the case of the  $(\text{OF})^{2-}$ .

The  $\text{O}^{\cdot-}$  center has the merit of relative simplicity providing thus a good opportunity to test some of the consequences of the cluster Jahn-Teller theory. The main reason for the relative simplicity is the fact that the free  $\text{O}^{\cdot-}$  ion possesses a separation of about  $100\,000 \text{ cm}^{-1}$  between the  $2p^5$  ground state and the first excited configuration given by  $2p^43s$ .

In Sec. II some information concerning the sample

TABLE I. EPR parameters of the  $O^-$  center and, for comparison, of the  $(OF)^{2-}$ . The constants are all related to the system of axes and the numbering of the nuclei as depicted in the Fig. 1. The hf constants are all in G.

	Oxygen ( $^{17}O$ )		Fluorine 1,2		Fluorine 3 <sup>a</sup>				
	$g_{\parallel} = g_{\perp}$	$g_{\perp} = g_{xx} = g_{yy}$	$A_{\parallel} A_{\perp}$	$A_{\perp} = A_{xx} = A_{yy}$	$A_{\parallel} = A_{\perp}$	$A_{\perp} = A_{xx} = A_{yy}$	$A_{xx}$	$A_{yy}$	$A_{\perp}$
	$\pm 0.001$	$\pm 0.001$	$\pm 1$		$\pm 0.5$				
$CaF_2 : O^-$ <sup>b</sup>	1.9955	2.1047	97.8	9 $\pm$ 6	63.6	15.4 $\pm$ 0.5	3.6 $\pm$ 0.5	1.2 $\pm$ 0.8	3.4 $\pm$ 0.5
$SrF_2 : O^-$ <sup>c</sup>	1.9895	2.1352			35.2	4 $\pm$ 2			
$CaF_2 : (OF)^{2-}$ <sup>d</sup>	2.0016	2.0458	104.5	20 $\pm$ 2	53.7	15 $\pm$ 2			

<sup>a</sup>The constants of the fluorines 4, 5, 6 are obtained from the ones of 3 by successive rotations by  $\frac{1}{2}\pi$  around the  $z$  axis.

<sup>b</sup>Reference 15,  $T = 4.2$  °K.

<sup>c</sup>Present paper,  $T = 4.2$  °K.

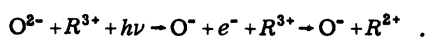
<sup>d</sup>Reference 10,  $T = 78$  °K.

preparation is given. Section III reviews some previously obtained features of the  $O^-$  center and introduces an application of the cluster Jahn-Teller theory to the present case. Finally, the experimental results given in Secs. IV and V are compared with the consequences of the model.

## II. EXPERIMENTAL DETAILS

The crystals investigated originated partly from the Materials Science Center at Cornell University and partly from Laboratoire PCS, University of Geneva. As the sample preparation is not totally trivial we review some essential points:

- (i) "Optran Grade"  $CaF_2$  powder<sup>11</sup> was used for crystal growing.
- (ii) Small amounts of various rare earths were introduced into the melt to serve as electron traps in the later conversion of  $O^{2-}$  to  $O^-$ . Care was taken to grow the crystals in an oxygen-free atmosphere. Oxygen present at this stage of preparation would invariably associate with the rare earth to form cluster centers<sup>12</sup> which give, after x-raying, very strong background signals.
- (iii) The samples were usually obtained by cleavage from the crystals. The specimens involved in the uniaxial-stress experiments were cut to shape, oriented by x rays, and then subsequently doped with oxygen and afterwards ground to dimensions.
- (iv) The samples were doped with oxygen by heating them in a sealed quartz ampoule. The  $(OH)^-$  freed at high temperatures by the walls of the quartz ampoule react with the sample by the hydrolysis reaction (Bontinck),<sup>13</sup> and diffusion of individual  $O^{2-}$  ions into the crystal results. Occasionally the crystals were heated in an open quartz tube with ultrapure argon flowing through the tube.
- (v) Subsequent x-raying of the specimen converts the  $O^{2-}$  into  $O^-$  according to



Due to the thermal treatment described above the oxygen and the rare-earth ions ( $R$ ) are located randomly with respect to one another. This has

been verified by examining the  $O^-$  centers in crystals with strongly different concentrations of rare earth and of oxygen.

EPR measurements were performed on a homodyne X-band spectrometer with a balanced mixer using backward diode detectors and 35- or 700-Hz modulation frequency. For part of the experiments the spectrometer was wired to produce the second derivative of the signal.

The intensity of the microwave field in the  $TE_{011}$  high-Q cavity was determined by measuring the saturation of the  $O_2^-$  in KCl and comparing with Castner's results,<sup>14</sup> by direct calculation, and by measuring the linewidth of  $Mn^{2+}$  in MgO at 4.2 °K. The value determined is  $H_1 = 4.5$  G at full incident microwave power (500 mW), or 0 dB in Fig. 9.

Usually the signal proportional to  $H_1 \partial \chi'' / \partial H_0$  was recorded on an  $xy$  recorder. The  $x$  axis was fed with a voltage proportional to the magnetic field  $H_0$ . Care was taken to avoid modulation broadening and fast-passage effects on the lines recorded. Temperatures were measured with a precalibrated Allen-Bradley resistor.

## III. MODEL

### A. Structure of center

In this section we briefly review previously obtained results.<sup>15</sup> The structure of the center consistent with them is depicted in Fig. 1. The  $O^-$  ion is paramagnetic and paraelastic. Its EPR spectrum implies an axial  $g$ -tensor, hyperfine interaction with two equivalent  $F^-$  neighbors along a fourfold crystal axis, for example, nuclei 1,2 in Fig. 1, and weaker hyperfine interaction with four  $F^-$  nuclei lying in the plane perpendicular to the axis. Table I summarizes the EPR data described by a conventional tetragonal spin Hamiltonian. Under the influence of uniaxial stress applied along a fourfold crystal axis, the center preferentially reorients with the  $g$ -tensor axis *parallel* to the stress. The reorientation time is too small to be measured by the method given by Känzig.<sup>16</sup> As discussed

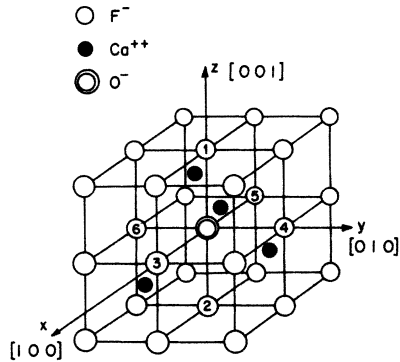


FIG. 1. Model of the  $O^-$  center as deduced from the experimental results. The tetragonal distortion is along  $[100]$ ,  $[010]$ , or  $[001]$ .

later, broadening of the spectral components by reorientation is observed in the range of liquid helium to 25 K. No motionally averaged spectrum is observed at higher  $T$ .

#### B. Formulation of Jahn-Teller model for center

The stress data to be discussed below and the EPR results show the  $O^-$  ion as interacting dominantly with tetragonally oriented lattice distortions through the Jahn-Teller effect. To simplify the model to a tractable form we approximate the dominant strain deformation by one pair of displacement coordinates,  $Q_\alpha$  and  $Q_\beta$ , transforming, respectively, as  $(3z^2 - r^2)$  and  $(x^2 - y^2)$  of the  $E$  representation of the cubic group. In the isolated cluster formed by the  $O^-$  and the six  $F^-$  neighbors they would correspond to the  $E_g$  normal modes as given by Van Vleck.<sup>17</sup> Under the simplifying assumption concerning the local strain field the model of the center is given by an electronic orbital triplet interacting through the tetragonal Jahn-Teller term with this pair of lattice displacements including their kinetic and potential energy. The joint motion of the coupled system is then perturbed by the spin-orbit coupling, the Zeeman and the hyperfine interaction of the magnetic electrons, and by the coupling to externally induced and to small random internal static strains.

The coupled motion of the model system in absence of spin-orbit coupling has been solved exactly by Moffit and Thorson<sup>18</sup> and by Ham.<sup>8</sup> The essential results of their calculations are briefly reviewed; the degeneracy of the triplet is not lifted by the Jahn-Teller term, the kinetic and potential lattice energies and the Jahn-Teller coupling term being simultaneously diagonal in the electronic states, and in the oscillator states with a suitably displaced origin. The Jahn-Teller interaction merely produces three local distortions of the surroundings of the  $O^-$  ion parallel to the fourfold

crystal direction. This is most easily visualized in the space of the  $Q_\alpha$ ,  $Q_\beta$  with the potential energy of the complex as the third dimension. The potential well having its origin at  $(0, 0)$  in the absence of the Jahn-Teller interaction is shifted to three positions given by

$$(Q_\alpha^0, Q_\beta^0) = \frac{2E_{JT}}{V_J} (\cos \frac{2}{3} \pi k, \sin \frac{2}{3} \pi k), \quad k=1, 2, 3 \quad (1)$$

where  $V_J$  is the Jahn-Teller coupling coefficient. This is depicted in Fig. 2 where  $E_{JT}$ , the Jahn-Teller energy, is defined. Within this model no off-diagonal matrix elements exist. Thus the wells behave each one as an independent entity.

The energy levels and eigenfunctions are given by

$$\begin{aligned} |x'\rangle &= |x\rangle |n_\alpha 1\rangle |n_\beta 1\rangle, \\ |y'\rangle &= |y\rangle |n_\alpha 2\rangle |n_\beta 2\rangle, \\ |z'\rangle &= |z\rangle |n_\alpha 3\rangle |n_\beta 3\rangle, \\ E_k &= E_0 + (n_\alpha + n_\beta + 1) \hbar\omega - E_{JT}, \quad k=1, 2, 3. \end{aligned} \quad (1a)$$

$E_0$  is the energy of the electronic ground state before switching on the JT effect. The  $n_\alpha, n_\beta$  are occupation numbers of the harmonic oscillators  $\alpha, \beta$ .  $|n_\alpha 1\rangle$  is the harmonic-oscillator wave function of occupation  $n_\alpha$  located in the potential well 1, etc. Finally,  $|x\rangle, |y\rangle, |z\rangle$  are the  $p$  functions serving as the basis of the  $T_1$  electronic ground state. The three ground-state levels are all shifted by the same amount, the Jahn-Teller energy. Irrespective of the strength of the interaction the

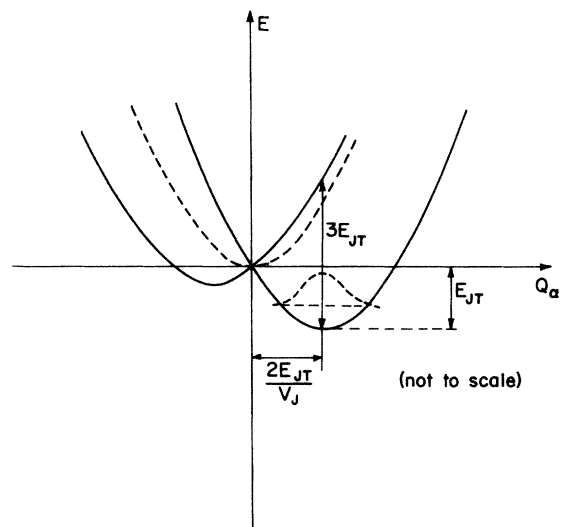


FIG. 2. Intersection of the energy surface  $E(Q_\alpha, Q_\beta)$  with the  $(E, Q_\alpha)$  plane. The potential consists of three disjoint paraboloids of revolution with minima as given by Eqs. (1) and (1a).

TABLE II. The matrix resulting from the action of  $\mathcal{H}_{\text{pert}}$  on the vibronic ground states.

$ x'_0 \rangle$	$ x'_0 \rangle$	$ y'_0 \rangle$	$ y'_0 \rangle$	$ z'_0 \rangle$	$ z'_0 \rangle$
$g_{\perp}\mu n_3 + V_1$	$(g_{\parallel}n_1 - ig_{\perp}n_2)\mu$	$-\frac{1}{2}if\lambda - fV_T\epsilon_{xy}$	0	$-fV_T\epsilon_{xx}$	$\frac{1}{2}f\lambda$
$(g_{\parallel}n_1 + ig_{\perp}n_2)\mu$	$-g_{\perp}\mu n_3 + V_1$	0	$+\frac{1}{2}if\lambda - fV_T\epsilon_{xy}$	$-\frac{1}{2}f\lambda$	$-fV_T\epsilon_{xx}$
$+\frac{1}{2}if\lambda - fV_T\epsilon_{xy}$	0	$g_{\perp}\mu n_3 + V_2$	$(g_{\perp}n_1 - ig_{\parallel}n_2)\mu$	$-fV_T\epsilon_{yy}$	$-\frac{1}{2}if\lambda$
0	$-\frac{1}{2}if\lambda - fV_T\epsilon_{xy}$	$(g_{\perp}n_1 + ig_{\parallel}n_2)\mu$	$-g_{\perp}\mu n_3 + V_2$	$-\frac{1}{2}if\lambda$	$-fV_T\epsilon_{yy}$
$-fV_T\epsilon_{xx}$	$-\frac{1}{2}f\lambda$	$-fV_T\epsilon_{yy}$	$\frac{1}{2}if\lambda$	$g_{\parallel}\mu n_3 + V_3$	$g_{\perp}\mu(n_1 - in_2)$
$\frac{1}{2}f\lambda$	$-fV_T\epsilon_{xx}$	$\frac{1}{2}if\lambda$	$-fV_T\epsilon_{yy}$	$g_{\perp}\mu(n_1 + in_2)$	$-g_{\perp}\mu n_3 + V_3$

with  $\mu = \frac{1}{2}\mu_B |B|$ ,  
 $V_1 = \frac{1}{2}V_E(\epsilon_a - \sqrt{3}\epsilon_\beta)$ ,  
 $V_2 = \frac{1}{2}V_E(\epsilon_a + \sqrt{3}\epsilon_\beta)$ ,  
 $V_3 = -V_E\epsilon_\alpha$ ,

$f = e^{-3E_J T/2\hbar\omega}$ ,  
 $g_{\perp} = g_e + \Delta g$  with  $\Delta g$  given by (2a),  
 $\epsilon_\alpha = \frac{1}{2}[2\epsilon_{zz} - (\epsilon_{xx} + \epsilon_{yy})]$ ,  
 $\epsilon_\beta = \frac{1}{2}\sqrt{3}(\epsilon_{xx} - \epsilon_{yy})$ ,

All terms which are very small (from the Ham theory) with respect to  $|\lambda f|$  or which shift all of the levels the same amount have been neglected.

first excited states are the finite amount  $\hbar\omega$  above the ground state.

The following electronic perturbations act within the vibronic ground states designated by  $|x'_0\rangle$ ,  $|y'_0\rangle$ ,  $|z'_0\rangle$ :

$$\mathcal{H}_{\text{pert}} = \lambda \vec{L} \cdot \vec{S} + \mu_B \vec{B} \cdot (\vec{L} + g_e \vec{S}) + \mathcal{H}_{\text{hf}}$$

$$+ V_E \left\{ \frac{3}{4} (\epsilon_{xx} - \epsilon_{yy}) (L_x^2 - L_y^2) + \frac{1}{4} (2\epsilon_{zz} - \epsilon_{xx} - \epsilon_{yy}) \right.$$

$$\left. \times [3L_x^2 - L(L+1)] \right\} + V_T [\epsilon_{xy} (L_x L_y + L_y L_x) + \dots].$$

These terms are, respectively, the spin-orbit coupling, electronic Zeeman effect, hyperfine interaction with the  $F^-$  neighbors, and interaction with the tetragonal and trigonal components of the elastic strain field. The matrix resulting from the action of  $\mathcal{H}_{\text{pert}}$  on the vibronic ground states is of order six (neglecting the hyperfine structure) and is given in Table II.  $V_E$  and  $V_T$  give the coupling of electronic states to the tetragonal and trigonal components, respectively, of the macroscopic strain with components  $\epsilon_{ij}$ . The magnetic field  $\vec{B}$  has direction cosines  $n_1, n_2, n_3$  with respect to  $x, y, z$  of Fig. 1,  $z$  being the axis of quantization of  $\vec{S}$ . The parameter  $f$  is the Jahn-Teller reduction factor. This is essentially the overlap integral between the vibrational part of two ground-state wave functions centered in different potential wells. Terms of second or higher order arise due to the nearby excited vibronic states of the system giving, in the limit of strong JT interaction, important contributions as has been shown by Ham.<sup>8</sup> For our system the important term of this sort is the perpendicular  $g$  shift,

$$g_{\perp} - g_e = (2|\lambda|/3E_{JT}) |\langle i|L_j|k\rangle|^2. \quad (2)$$

The matrix element represents a suitable compo-

nent of  $\vec{L}$  in the electronic triplet ground states, and is either 1 or 0 in a pure crystal-field model. In the present case the covalency is not negligible but in order to keep a manageable model we have taken this into account in a rather crude fashion by determining the value of the matrix element from the hyperfine-structure data. The value thus found is  $|\langle i|L_j|k\rangle| = 0.94$ . For reasons analogous to those just given the  $g_{\parallel}$  value in the matrix is defined as the measured  $g_{\parallel}$  and not as  $g_e = 2.0023$  as given by the Moffitt-Thorson-Ham model.

In principle one should consider the generalization of the matrix in Table II to include the degrees of freedom associated with the nuclear spins of the six  $F^-$  neighbors which give rise to a partially resolved hyperfine structure. For the sake of brevity we do not consider explicitly here the possible reorientation mechanisms associated with off-diagonal elements of this hyperfine interaction since they can be argued to be insignificant.

#### IV. STATIC PROPERTIES

##### A. Stress measurements

The interaction between the strain acting upon the center and its electronic ground state is given by the last terms of  $\mathcal{H}_{\text{pert}}$  within a linear theory. The part of this interaction transforming as  $E$  gives diagonal terms in the matrix (Table II) and is thus not altered by the Jahn-Teller distortion. The  $T_2$  part, however, being off diagonal is multiplied by the Jahn-Teller reduction factor  $f$  and is quenched. By introducing the usual linear stress-strain relation into these terms the level splitting for different directions of applied uniaxial stress can be calculated. Stress applied parallel to  $[110]$  or  $[001]$

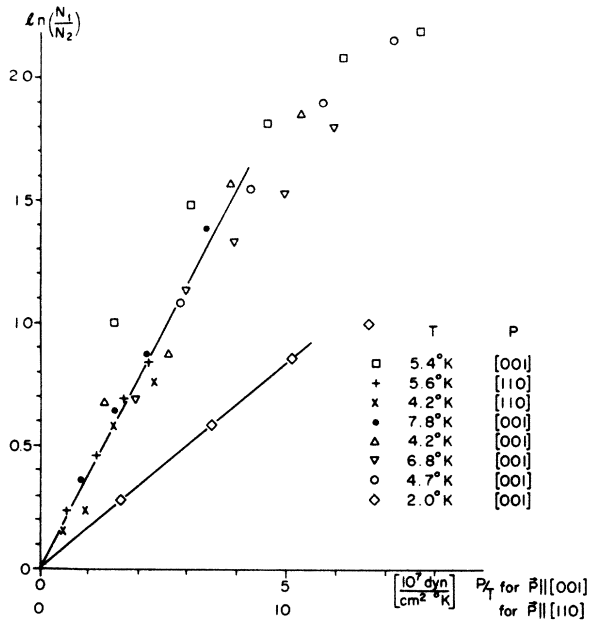


FIG. 3. Natural logarithm of the ratio of the integrated intensities for those centers with axes parallel (or at 45° for  $P \parallel [110]$ ) to the applied stress relative to those with axes perpendicular as a function of  $P/T$ . Note the different scale for the [110] data.

yields an orientational doublet and singlet. The ratio of the stress induced splitting for these two cases is predicted to be  $\Delta E_{[001]} : \Delta E_{[110]} = 2 : 1$ , assuming  $|\epsilon V_E| > |g\mu_B \vec{B}|$ , as well as  $|V_E| \gg |fV_T|$ .

Measurements of the relative occupation numbers of the levels have been performed for these two directions of applied stress by using the technique described by Känzig.<sup>16</sup> The results are depicted in Fig. 3. The measurements with  $P \parallel [110]$  have been entered with a reduced  $P/T$  scale to test the scaling predicted by the model. The fact that, for  $P/T \leq 4 \times 10^7$  dyn/cm<sup>2</sup> °K, the points for both stress directions are distributed along one straight line is

a further confirmation of the tetragonal symmetry of the center.

Note that the  $\text{CaF}_2 : \text{O}^-$  center behaves under stress differently from the usual behavior for orientable molecules. The center has its minimum energy when aligned with  $g_{\parallel}$  parallel to the stress, whereas the more usual case exhibits minimum energy with the unique  $g$  axis perpendicular to the applied uniaxial stress.

The stress-coupling coefficient as determined from the slope of the straight line is given in Table III. Besides the usual errors involved in the determination of stress and temperature, rather large uncertainties occurred in the double integration of the recorded first derivative spectra due to the sensitivity of the line shape to applied stress. Rather large changes in the wings arise under applied stress as will be discussed below.

The markedly different slope of the stress results performed at 2°K, as shown in Fig. 3, is attributed to the presence of small random internal strains acting upon the centers. It is certainly not due to saturation effects as all the measurements have been performed under nonsaturation conditions. The effect arises when the temperature of measurement is of the order of the energy splittings produced by the internal-strain distribution.

To obtain a better qualitative insight, the population ratio

$$\beta = (N_3 - N_2 - N_1) / (N_3 + N_2 + N_1)$$

has been calculated under the following assumptions:  $N_1, N_2, N_3$  represent the probability of the center to be oriented along, respectively,  $x, y, z$  of Fig. 1. Neglecting the Zeeman splitting of each of the Kramers doublets, only the linear interaction with tetragonal strain and with uniaxial stress applied parallel to  $z$  has been considered. The distributions of the strain interaction energies  $V_E \epsilon_{\alpha}$  and  $V_E \epsilon_{\beta}$  have been approximated by Lorentzians of half-width  $\alpha$  (Stoneham).<sup>19</sup> By applying Boltzmann statistics the value of  $\beta$  has been calculated to be

$$\beta = \left(\frac{\delta}{\pi}\right)^2 \int_{-\infty}^{+\infty} \int_{-\infty}^{+\infty} dx_1 dx_2 \left[ \tanh\left(\frac{3}{4} \frac{PV_E(S_{11} - S_{12})}{kT} + \frac{3}{4} x_1 - \frac{1}{2} \ln \cosh \frac{1}{2} \sqrt{3} x_2 - \frac{1}{2} \ln 2\right) / (x_1^2 + \delta^2)(x_2^2 + \delta^2) \right]. \quad (3)$$

The variables of integration are  $x_1 = V_E \epsilon_{\alpha} / kT$ ,  $x_2 = V_E \epsilon_{\beta} / kT$ , and the reduced width of the strain distribution is  $2\delta = 2\alpha / kT$ . The expression (3) has been evaluated by computer.

By fitting the calculations to the experimental results of Fig. 4 our estimate of the width of the distribution strain energies is obtained. The value  $2\delta$  calculated is equivalent to  $2\alpha = 2.6$  cm<sup>-1</sup>. Some stress measurements have been performed with  $P$

applied parallel to a trigonal crystal axis. No change in the relative line heights nor of the total integrated area under the spectrum was detected within experimental precision. This absence of any observable effects due to  $T_2$ -type applied strains is a very satisfactory result in view of the reduction of the trigonal coupling predicted by the model of the Jahn-Teller effect chosen to describe this center.

## B. Line shape

All of the EPR lines of the center exhibit pronounced asymmetry in their shape. At zero external stress they show a more usual low-field side and a high-field part slowly trailing off, as may be seen by inspecting Fig. 5.

Uniaxial stress applied to the crystal produces narrowing of the lines and their shape becomes more symmetrical. Figure 6, presenting a second-derivative spectrum of enhanced resolution, demonstrates this process of narrowing particularly well. Further, a dramatic enhancement of the total integrated intensity of the observed spectrum is ob-

served for applied tetragonal stress large compared to the random internal stresses.

The model of the center as discussed in Sec. III in conjunction with the assumption of a static strain-field distribution is able to account for the observed line shape through its prediction of a stress-dependent part of the experimental  $g$  values. The tetragonal component of the strain field at any particular site is specified by a point in the  $\epsilon_\alpha, \epsilon_\beta$  plane sketched in Fig. 7. In the regions of Fig. 7 exclusive of I and II, defined by  $|V_i - V_k \pm g\mu_B B| > |f\lambda|$  for  $i=3, k=1, 2$ , and for  $B$  parallel to a fourfold crystal axis, the experimental  $g$  values may be calculated by perturbation theory from the Hamiltonian of Table II and are

$$g_{\parallel \text{exp}} = g_{\parallel} - \frac{1}{4}f^2\lambda^2 (g_{\parallel} + g_{\perp}) \left( \frac{1}{(V_1 - V_3)^2 - \frac{1}{4}(g_{\parallel} + g_{\perp})^2 \mu_B^2 B^2} + \frac{1}{(V_2 - V_3)^2 - \frac{1}{4}(g_{\parallel} + g_{\perp})^2 \mu_B^2 B^2} \right), \quad (4a)$$

$$g_{\perp \text{exp}}^{(1)} = g_{\perp} - \frac{1}{4}f^2\lambda^2 (g_{\parallel} + g_{\perp}) \left( \frac{1}{(V_1 - V_3)^2 - \frac{1}{4}(g_{\parallel} + g_{\perp})^2 \mu_B^2 B^2} \right), \quad (4b)$$

$$g_{\perp \text{exp}}^{(2)} = g_{\perp} - \frac{1}{4}f^2\lambda^2 (g_{\parallel} + g_{\perp}) \left( \frac{1}{(V_2 - V_3)^2 - \frac{1}{4}(g_{\parallel} + g_{\perp})^2 \mu_B^2 B^2} \right). \quad (4c)$$

Note that conventional contributions to the  $g$  shift which are first order in  $\lambda$  are negligibly small because of the reduction of the orbital Zeeman matrix elements by the Jahn-Teller effect. One may similarly, in principle, calculate the experimentally observed  $g$ 's for regions I and II in Fig. 7 where one or another of the results above, Eq. (4), is no longer valid. The observed line is finally the superposition of the lines corresponding to each value of strain ( $\epsilon_\alpha, \epsilon_\beta$ ) weighted by a factor expressing the stress distribution, with an additional breadth due to the unresolved hyperfine interactions with near and further  $F^-$  neighbors.

The experimental lines are dominated by sites with local strain corresponding to those regions outside I or II, or both, depending upon the line in question. As ( $\epsilon_\alpha, \epsilon_\beta$ ) approaches the boundary of I and/or II, two (or all three) of the  $g$  shifts become large and negative; it is these regions in ( $\epsilon_\alpha, \epsilon_\beta$ ) which contribute to the high-field (low- $g$ ) tail of the observed lines. Detailed investigation of the solutions in regions I and II indicates that the resulting  $g$  values (resonant fields) are distributed over such a wide range of values that this part of the ( $\epsilon_\alpha, \epsilon_\beta$ ) distribution does not contribute to the experimentally observed lines.

Figure 7 is helpful in understanding the effects of an applied stress upon the observed spectrum. For these arguments, the strain distribution is represented crudely by a uniform distribution within a circle of radius ( $\alpha/V_B$ ) and zero outside. For

zero applied stress this region is centered at the origin and denoted by III in Fig. 7, while for large stress applied parallel to [010] it is displaced as indicated by region IV. As may be seen in Fig. 7, (a) the application of a stress reduces the fraction of centers with strain near the boundaries of I and

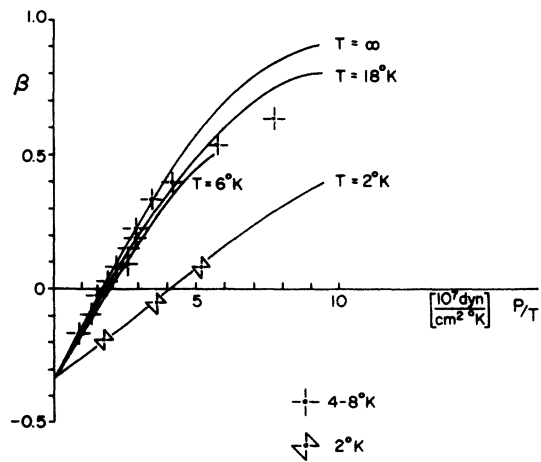


FIG. 4.  $\beta$ , as defined in the text before Eq. (3), as a function of  $P/T$ . No distinction is made among the points for  $4^\circ\text{K} < T < 8^\circ\text{K}$  since in this temperature range the results are not sensitive to the presence of internal strains. The curves are the results of Eq. (3) using the value  $\alpha = 1.3 \text{ cm}^{-1}$ .

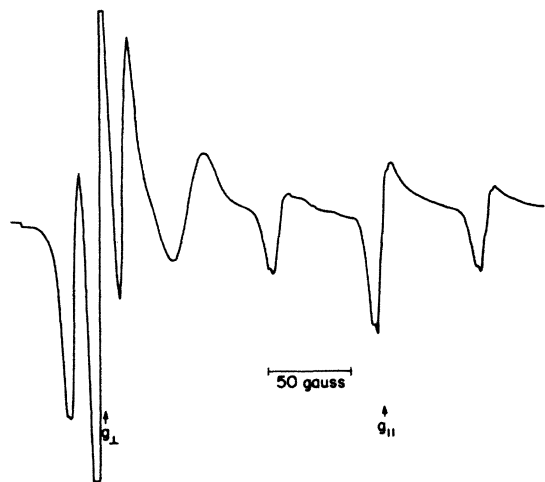


FIG. 5. First-derivative EPR absorption spectrum with  $\vec{B} \parallel \vec{C}_4$  axis in absence of applied stress. The spectrum consists of two sets ( $g$  anisotropy splitting) of three lines each (hyperfine splitting by two F nuclei). The central line of the seven is not associated with the  $O^-$  center. Note the marked line asymmetry resulting from the distribution of internal strain fields.

II which contribute to the high-field wings of the line, and thus the lines become more symmetric as is observed experimentally (Fig. 6); (b) the stress also reduces the fraction of centers in regions I and II which are unobserved, thus enhancing the total spectral intensity, again in accord with the experiments.

From these arguments one may, in fact, make rough estimates of the reduced spin-orbit coupling  $f\lambda$ . With a large stress applied parallel to axis 2 and with  $B$  parallel to axis 3, the repopulation implies that the spectrum is dominated by orientation 2, for which the energy denominator, Eq. (4c), is

$$g_{\parallel \text{exp}} = g_{\parallel} + \frac{(g_{\parallel} - g_{\perp}) V_T^2 f^2}{g_{\parallel}} \left( \frac{\epsilon_{xx}^2}{(V_3 - V_1)^2 - \frac{1}{4}(g_{\parallel} - g_{\perp})^2 \mu_B^2 B^2} + \frac{\epsilon_{yy}^2}{(V_3 - V_2)^2 - (g_{\parallel} - g_{\perp})^2 \mu_B^2 B^2} \right) \quad (5)$$

This expression does not lead to the experimentally observed line shape since it corresponds to a line trailing off slowly to the low rather than to the high field side, confirming the assumption that internal trigonal strain fields do not play an important role. Additional evidence for the relative lack of importance of the trigonal coupling is the experimental absence of a dependence of  $g_{\parallel}$  upon applied stress of trigonal symmetry, a dependence predicted by the above equation.

## V. DYNAMIC PROPERTIES

### A. Reorientation mechanisms

The center reorients even at low temperatures among the three available tetragonal positions as

defined by the applied strain. The distribution for this applied strain is represented by region IV of Fig. 7, and any loss of intensity from this line would be proportional to the intersection of regions II and IV which becomes zero as the applied stress becomes large. At zero stress, on the other hand, the contribution of the three orientations, now equally populated, is reduced by the intersection of II with III for orientation 2, I with III for 1, and of the union of I and II with III for 3. The radius of III and IV is determined from the  $\alpha$  of Sec. IV A to be  $\sim 6 \times 10^{-5}$ ; the half-width of strips I and II is determined from Eq. (4) and the cutoff used in the experimental determination of the line intensities, namely, 36 G. Relating these parameters as defined by the geometry of Fig. 7 to the observed stress enhancement of  $\times 2$  gives finally a rough estimate of  $f\lambda \sim 0.09 \pm 0.03 \text{ cm}^{-1}$ .

An independent measure of  $f\lambda$  may be obtained by noting that in the regime in which the applied stress is larger than the internal stresses, there is still a broadening of the lines resulting from the distribution of  $g$  values associated with the distribution of internal stresses via Eq. (4). Knowing the range of internal stress interactions,  $2\alpha$ , and the stress dependence of the linewidth allows the rough estimate  $f\lambda = 0.11 \pm 0.04 \text{ cm}^{-1}$ , in satisfactory agreement with the estimate from the enhancement.

The discussion of this section relies upon assuming that  $|f\lambda| \gg |fV_T \epsilon_{ik}|$ , or that the off-diagonal elements in (2) are dominated by spin orbit, not trigonal strain terms. If the reverse condition is valid, a  $g_{\parallel}$  ( $B$  assumed parallel to a fourfold crystal axis) calculated under the assumption

$$|V_i - V_j \pm g\mu_B B| > |fV_T \epsilon_{ij}|$$

is given by

has been demonstrated by the stress measurements. This section gives some theoretical considerations connecting this feature with the saturation and linewidth measurements as given in Sec. VB.

The vibronic ground state of the center has been shown to be split by random static tetragonal strain. This splitting localizes the different orientations. However, as the matrix, Table II, is not diagonal the localized states are not eigenstates of the Hamiltonian. In general, these eigenstates are linear combinations of all of the six localized basis states, the spin-orbit term being dominant in the mixing of these states. The thermal phonon field in the crystal randomly modulates the local

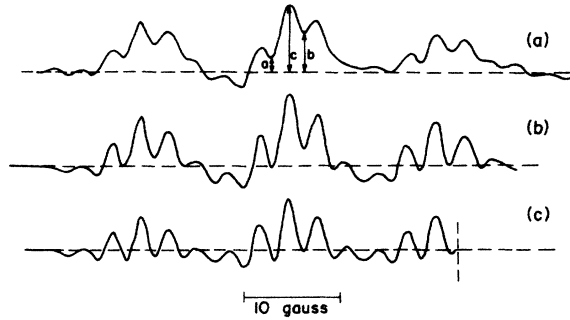


FIG. 6. Second derivative of the  $g_1$  component of the spectrum with  $\vec{B} \parallel [110]$  axis. The principal triplet splitting results from the hyperfine interaction with fluorine 1 and 2 of Fig. 1, and the barely resolved five-line structure is the hyperfine interaction with the remaining four fluorine nuclei. The spectra are for three values of the applied stress, parallel to  $[001]$ . The ratio  $(b-a)/c$ , with  $a$ ,  $b$ ,  $c$  as defined in the figure, is taken as a measure of the line asymmetry and is given below for the different stresses. Note also the increased resolution at the higher stress (because of repopulation with stress, the spectrometer gain is reduced in going from  $a$  to  $c$ ):

Spectrum	$P(10^8 \text{ dyne/cm}^2)$	$(b-a)/c$
$a$	0	0.4
$b$	1.5	0.22
$c$	2.7	0.16

strain acting upon the center. This time-dependent Hamiltonian  $\mathcal{H}(t)$  possesses nonzero matrix elements between the eigenstates of the matrix of Table II and thus induces transitions. Decomposition of the fluctuating strain according to the cubic symmetry yields (the  $A_1$  part is ineffective) a part transforming as  $E$  and a second one as  $T_2$ . They represent two different kinds of transition mechanisms. The first part being diagonal in the matrix of Table II has matrix elements between eigenstates in second order due to the mixing by the spin-orbit coupling, the anisotropic part of the electronic Zeeman effect, and the off-diagonal hyperfine interaction. The second part being off diagonal provides transitions already in first order. However, it is multiplied by the Jahn-Teller reduction factor. Note that the diagonal part modulates the splittings of the vibronic ground state, whereas the second part modulates the height of the potential well between the minima.

Potentially there is still another mechanism involved in inducing transitions between the eigenstates not accounted for up to now. The hyperfine interaction with the  $F^-$  neighbors contains a time-dependent contribution. The off-diagonal part of this term produces transitions between the partners of the Kramers doublets already in first order. However, this mechanism is probably too weak to be important.

We argue that the experimental results imply that the essential mechanism involved in the reorientation process is the spin-orbit coupling in conjunction with the tetragonal part of the time-dependent strain. To demonstrate this assertion the remainder of the section deals with the reorientation process under the assumption  $\vec{B} \parallel \vec{z}$  of Fig. 1. Neglecting hyperfine interaction and the static trigonal strain the matrix (2) splits into two independent blocks. Diagonalization of each leads to two sets of three states. One of these sets, to first order in the wave functions, is given by

$$\begin{aligned}
 |1\rangle &= \left( |x \pm\rangle \frac{if\lambda}{2(V_1 - V_2)} |y \pm\rangle \right. \\
 &\quad \left. \pm \frac{f\lambda}{2(V_1 - V_3) \pm (g_1 + g_{11}) \mu_B B} |z \mp\rangle \right), \\
 |2\rangle &= \left( \pm \frac{if\lambda}{2(V_1 - V_2)} |x \pm\rangle + |y \pm\rangle \right. \\
 &\quad \left. + \frac{if\lambda}{2(V_2 - V_3) \pm (g_1 + g_{11}) \mu_B B} |z \mp\rangle \right), \\
 |3\rangle &= \left( \pm \frac{f\lambda}{2(V_1 - V_3) \pm (g_{11} + g_1) \mu_B B} |x \pm\rangle \right. \\
 &\quad \left. + \frac{if\lambda}{2(V_2 - V_3) \pm (g_{11} + g_1) \mu_B B} |y \pm\rangle + |z \mp\rangle \right),
 \end{aligned} \quad (6)$$

where the upper signs are to be chosen throughout. The second set of states,  $|4\rangle$ ,  $|5\rangle$ ,  $|6\rangle$ , is given by choosing the lower signs. The  $E$  part of the time-dependent strain has matrix elements only within each of the groups and, though providing relaxation within either group, cannot induce transitions from one group to the other.

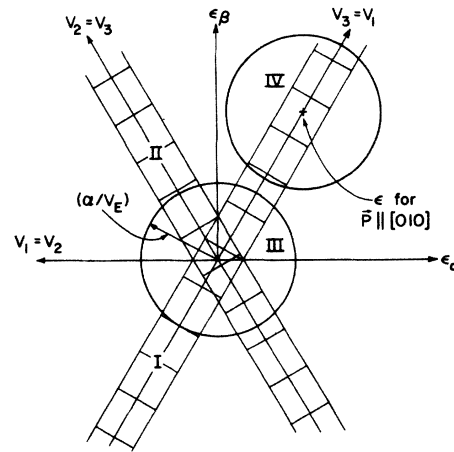


FIG. 7. The  $(\epsilon_\alpha, \epsilon_\beta)$  plane and regions of validity of Eqs. (4) of text: region I—Eqs. (4a) and (4b) invalid; II—Eqs. (4a) and (4c) invalid; III—(area within circle) representation of distribution of internal strains; IV—the same, but the presence of an applied uniaxial stress along the  $y$  (or 2) axis.

The physical meaning is that the  $T_1 \otimes S$  space is split into two halves each having three basis states, each of the three states corresponding roughly to deformation of the center along a different one of the three fourfold crystal axes. The  $E$ -type strain provides for reorientations within the halves but not between them. This reorientation mechanism thus does not provide for a net spin flip without change of spatial orientation. From the point of view of EPR this behaves as a  $T_2$  relaxation mechanism. The trigonal time-dependent strain and the static and fluctuating off-diagonal parts of the hyperfine interaction couple the two halves of the  $T_1 \otimes S$  space and thus can provide for the possibility to flip a spin without spatial reorientation. They enable  $T_1$  relaxation.

The spin-orbit induced reorientation transition between the levels (6) will now be calculated. The transition probability  $W_{ik}$  between the levels  $i$  and  $k$ , split in energy by an amount  $\Delta_{ik}$ , is readily obtained by following the arguments developed by Sussman<sup>20</sup> and Pirc *et al.*<sup>21</sup> The phonon spectrum taken in the long-wavelength approximation is assumed to be given by a Debye density of states. The resulting expression is

$$W_{ik} = \frac{9}{32\pi} \frac{V_E^2 (f\lambda)^2}{\hbar^4 \rho} \sum_{\mu} \left\langle \frac{(G_{\mu}^{ik})^2}{S_{\mu}^5} \right\rangle \times \frac{\Delta_{ik}}{\exp(-\Delta_{ik}/k_B T) - 1}, \quad (7)$$

with

$$G_{\mu}^{ik} = (\vec{a}_{\mu} \cdot \vec{e}_i)(\vec{k}_e \cdot \vec{e}_i) - (\vec{a}_{\mu} \cdot \vec{e}_k)(\vec{k}_e \cdot \vec{e}_k).$$

The phonons are described by wave vectors  $\vec{k}$ , branch  $\mu$  with polarization vector  $\vec{a}_{\mu}$ , and velocity  $S_{\mu}(\vec{k})$ ; the  $\vec{e}_i$  are unit vectors referred to the center axes given in Fig. 1;  $\vec{k}_e = \vec{k}/|k|$ ;  $k_B$  is the Boltzmann constant. The average is taken over directions of the propagation vector  $\vec{k}$ . In the limit  $\Delta_{ik}/k_B T \ll 1$ , expression (7) becomes independent of  $\Delta_{ik}$  and linear in temperature. Further, as the crystal is cubic,

$$\langle (G_{\mu}^{12})^2 \rangle = \langle (G_{\mu}^{23})^2 \rangle = \langle (G_{\mu}^{31})^2 \rangle$$

and  $W_{ik}$  is the same for all pairs of levels. The formula derived from (7) giving the mean lifetime  $T_2$  of the center in one of the three states is ( $\Delta_{ik}/k_B T \ll 1$ )

$$\frac{1}{T_2} = 2W_{ik} = \frac{9}{16\pi} \frac{V_E^2 f^2 \lambda^2 k_B T}{\hbar^4 \rho} \times \sum_{\mu} \left\langle \frac{(G_{\mu}^{ik})^2}{S_{\mu}^5} \right\rangle. \quad (8)$$

This time is the same for both triplets, of course.

Consider now the relaxation processes connecting the two halves of the  $T_1 \otimes S$  space which must

arise from processes other than that discussed above. Only their functional dependence is discussed. The one-phonon transition probability due to mixing by the static hyperfine interaction has the same dependence on the appropriate level splitting (approximately  $|g\mu_B B|$ ) and temperature as (7). The contributions due to the time-dependent trigonal strain and the fluctuating off-diagonal hyperfine terms involve a transition probability proportional to  $(fV_T)^2 \Delta_{ik}^2 T$  (for  $\Delta/k_B T < 1$ ), in the first case  $\Delta_{ik}$  being the static strain splitting. The hyperfine mechanism goes with  $\eta^2 (g\mu_B B)^2 T$ , with  $|g\mu_B B|$  being the Kramers double splitting and  $\eta$  representing a properly chosen part of the time-dependent hyperfine tensor.

When  $B$  is pointing in an arbitrary direction, in contrast with the situation with  $\vec{B} \parallel \vec{C}_4$ , the matrix (2) no longer decomposes into two blocks. The transformation of (2) by choosing the axis of quantization of  $S$  parallel to  $B$  yields nonzero spin-orbit matrix elements connecting any two states with the exception of the Kramers conjugated pairs. A nondiagonal electronic Zeeman term proportional to  $(g_{\perp} - g_{\parallel})$  and an off-diagonal hyperfine interaction connect these latter ones but mechanisms involving these terms are smaller than the spin-orbit-dependent one. Correspondingly, pairs or chains of reorientation events involving the spin-orbit process override in general the reorientations or spin flips due to the hyperfine and  $g$ -anisotropy mechanisms. Thus, for a general direction of  $\vec{B}$  the spin-orbit-induced jumps contribute to  $T_2$  and  $T_1$  relaxation, whereas for  $\vec{B} \parallel \vec{C}_4$  they contribute only to  $T_2$ . For the general orientation the total transition probability from a given level is still given by (7), the partition into spin-flip and spin-preserving reorientations being given by appropriate angular factors.

It is meaningful to think of these reorientation processes as being described by a Markoffian probability function for the following reasons. The occurrence of the jumps is statistical, their duration is very short compared to the microwave period, whereas the time the center remains in a given orientation is relatively long in the temperature interval of interest. The center thus corresponds to a very strongly hindered rotator with virtually no correlation between consecutive jumps. The reorientation process provides for jumps between the different lines of the EPR spectra. To be specific,  $\vec{B} \parallel \vec{Z}$  (Fig. 1) is chosen. The spin-orbit coupling enables then the following paths:

$$|1 \pm\rangle \leftrightarrow |3 \mp\rangle \leftrightarrow |2 \pm\rangle \leftrightarrow |1 \pm\rangle$$

as discussed before. The first two steps involve changes in the  $g$  value as well as spin flip. They represent jumps between the perpendicular and the parallel EPR spectrum. The third path enables

jumps within the perpendicular spectrum. In all the processes two pairs of  $F^-$  nuclei have the magnitude of their respective hyperfine tensors changed. The mechanism thus also provides for jumps between the different hyperfine components.

As can be confirmed from the wave functions (6), these distortional reorientations are, in general, accompanied by a change in phase of the transverse component of  $\vec{S}$ . This fact precludes the straightforward application of the Anderson model<sup>22</sup> to the present case, as this model only involves stochastic changes of the precession frequency of the spin but no abrupt phase changes. The random-phase jumps in the previously discussed system are essential. They provide an ensemble average of the transverse magnetization decreasing in magnitude with increasing jump frequency. The fact that no motionally averaged EPR spectrum has been detected is attributed to this mechanism being active.

#### B. Experimental consequences of reorientation

In Sec. V A, the spin-orbit mechanism has been proposed as the most important reorientation mechanism for the  $\text{CaF}_2:\text{O}^-$  system. In this section a number of experimental results are discussed which seem to confirm this assertion.

First, the one-phonon nature of the relaxation process is indicated by a linewidth analysis of the experimental spectra. The lines exhibit at and below 4.2 °K an almost temperature-independent line shape with a nearly Gaussian low-field tail.

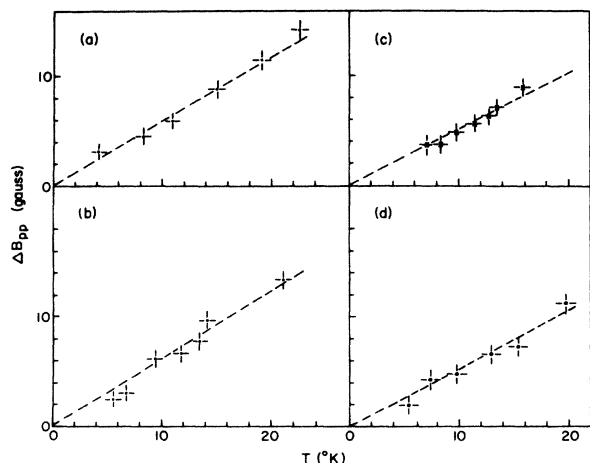


FIG. 8. Motionally induced Lorentzian contribution to the linewidth as a function of temperature: (a)  $\vec{B} \parallel \vec{C}_2$ , perpendicular spectrum,  $P=0$ ; (b)  $\vec{B} \parallel \vec{C}_2$ , perpendicular spectrum,  $P=1.7 \times 10^9$  dyne/cm<sup>2</sup> applied parallel to  $\vec{C}_4$ , perpendicular to  $\vec{B}$ ; (c)  $\vec{B} \parallel \vec{C}_3$ ,  $P=0$ ; (d)  $\vec{B} \parallel \vec{C}_4$ , perpendicular spectrum,  $P=0$ . The uncertainty in the slope for each plot is  $\sim \pm 0.18$  G/°K and the mean of the slopes is 0.57 G/°K.

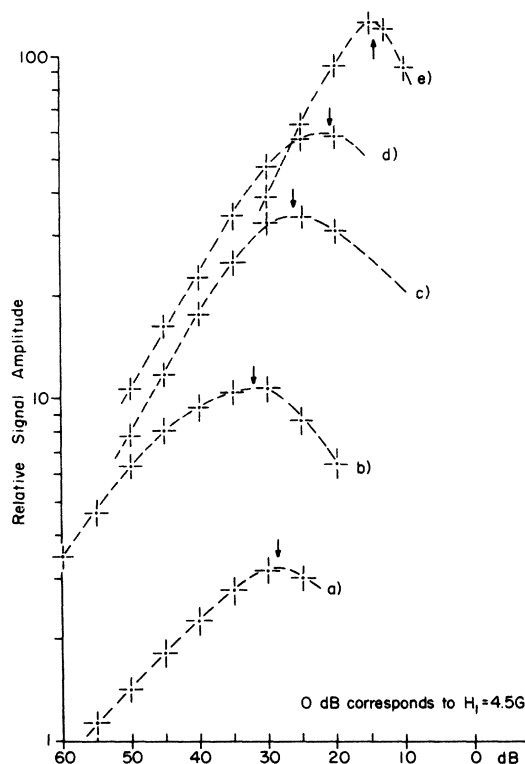


FIG. 9. EPR saturation plots. First-derivative peak-to-peak amplitude as a function of applied microwave power. Relative normalization of different curves is arbitrary: (a)  $\vec{B} \parallel \vec{C}_4$ , parallel spectrum,  $T=2$  °K; (b)  $\vec{B} \parallel \vec{C}_4$ , perpendicular spectrum,  $T=2$  °K; (c)  $\vec{B} \parallel \vec{C}_4$ , perpendicular spectrum,  $T=4.2$  °K; (d)  $\vec{B} \parallel \vec{C}_2$ , perpendicular spectrum,  $T=2$  °K; (e)  $\vec{B} \parallel \vec{C}_2$ , perpendicular spectrum,  $T=4.2$  °K.

At higher temperatures the lines take a more nearly Lorentzian low-field shape and they broaden due to the motional effects. This contribution as a function of temperature has been determined for several lines. Care has been taken to avoid any saturation. The results are depicted in Fig. 8 representing the peak-to-peak derivative of the Lorentzian contribution versus temperature. They have been obtained by decomposing the low-field part of the lines with the aid of the Voigt profile analysis.<sup>23</sup> The absolute precision of these results is not easily determined. The given errors are estimates based on the reproducibility from different samples. The uncertainty essentially arises from the uncertainty involved in the determination of the point corresponding to  $g=g_1$ . The main features of these measurements are linear temperature dependence below roughly 25 °K; independence of magnetic-field orientation within experimental precision; and slope of linewidth versus temperature is stress independent for  $T > 9$  °K.

The results are in accord with the proposed

mechanism, and in particular the absence of a stress dependence of the one-phonon rate is a characteristic of the phonon-assisted tunneling mechanism in contrast with others such as coupling to the phonons through the trigonal strain components. Using  $1/T_2 = \frac{1}{2}\sqrt{3}\gamma\Delta B_{LDP}$ , with  $\Delta B_{LDP}$  the peak-to-peak first-derivative width of the Lorentzian component of the line, the observed slope of 0.57 G/°K gives a  $T_2 T$  product of  $1.2 \times 10^{-7}$  sec °K.

No motionally narrowed spectrum is observed at higher temperature, consistent with the observation that the reorientation involves also a phase change of the transverse magnetization which destroys the possibility of developing a narrowed spectrum.

In addition to the line broadening with increasing temperature, there are line shifts describable by  $\delta g_{\parallel} = +9.8 \times 10^{-6} T^2$  and  $\delta g_{\perp} = -7.5 \times 10^{-6} T^2$ . Although suggestive of the shifts predicted by the Anderson theory, they are larger by a factor of  $\sim 12$  than one would predict from the measured widths and must be ascribed to some other mechanism. These shifts seem inexplicable in the framework implied by the effective Hamiltonian, Table II, and are the subject of further investigation.

Saturation measurements give further confirmation of the ideas proposed above. Figure 9 depicts some experimental saturation curves. They have been constructed by using the peak-to-peak height of the recorded first-derivative spectra. All of them with the exception of the one labeled *e* exhibit a shape differing quite sizeably from the theoretical one given by Castner.<sup>24</sup> The theory of Castner assumes a unique relaxation time characterizing the line. In the present case, however, a unique relaxation time applies only for those centers governed by relaxation processes underlying Eq. (8) in the limit  $\Delta_{ik}/kT \ll 1$ . At 4.2 °K this is true for most of the centers when  $\vec{B}$  is oriented in a general direction (curve *e* in Fig. 9). The maximum of the saturation curve involves some mean-relaxation-time representative for an important part of the centers. The position of this maximum is chosen as being representative in what follows.

Experimental support for the spin-orbit driven tunneling is obtained by comparing the saturation curves taken at a given temperature but with different directions of the magnetic field. A shift of 15 dB to lower  $\mu$ -wave power is observed by going from the curves corresponding to the magnetic field oriented along a twofold or threefold axis to the ones obtained with  $B \parallel [001]$ . By using  $T_2(C_2) = T_2(C_4)$  a ratio  $T_1(C_4):T_1(C_2) \cong 30:1$  is calculated from this result. This dramatic anisotropy is a natural consequence of the factorization of the matrix (2) into two blocks for the special orientations

$\vec{B} \parallel \vec{C}_4$ , as discussed in Sec. V A, and thus is consistent with the proposed spin-orbit mechanism. It would not be predicted by the other mechanisms discussed briefly above, one of which presumably is the source of the much weaker ( $\sim \times 30$ )  $T_1$  process for  $\vec{B} \parallel \vec{C}_4$ .

Also, the saturation plot gives qualitative confirmation of the dominance of one-phonon relaxation being involved. The curves corresponding to the same experimental conditions are shifted by  $\sim 7$  dB to higher microwave power when the temperature is raised from 2 to 4.2 °K. By using the one-phonon model a shift of 6.4 dB is calculated from the saturation parameters. At lower temperatures, however, where  $\Delta_{ik}/kT \gtrsim 1$  for an appreciable fraction of the centers, the reorientation rates depend upon the local strain and the EPR lines will be characterized by distribution of relaxation times.

Finally, the saturation data may be compared with the linewidth results. By choosing  $B \parallel [110]$  in Fig. 1, one obtains from the rate equations for this problem an effective  $T_1$  entering the saturation parameter which is  $T_1 = 2T_2$  for saturation of the transition  $|z+\rangle \leftrightarrow |z-\rangle$ . The saturation curves corresponding to this case are *d* and *e* of Fig. 9. These results then imply a value  $T_2 T = 2.1 \times 10^{-7}$  sec °K in rough accord with the  $T_2 T$  of  $1.2 \times 10^{-7}$  sec °K determined from the linewidth. The discrepancy may be due in part to extrapolation of the linear  $T$  dependence to temperatures which are comparable with the splittings due to internal strain fields and in part due to experimental problems with spectrometer linearity at high-power levels. The important point is that experimentally  $T_1$  and  $T_2$  are comparable in magnitude for  $\vec{B} \parallel [110]$ , a natural consequence of the spin-orbit mechanism. If one proposes separate mechanisms for reorientation and spin relaxation, then it is surprising that they should be finally comparable in magnitude.

The experimental value of  $T_2 T$  together with Eq. (8) gives the possibility to determine the reduced spin-orbit coupling constant  $f\lambda$ . The necessary parameters are  $V_E$  as given in Table III (it is assumed to be valid also for the low-frequency phonons involved in the reorientation mechanism); and  $\sum_{\mu} \langle (G_{\mu}^{ik})^2 / S_{\mu}^5 \rangle$  as given in Table III. It represents the average of  $G_{\mu}^{ik}$  taken over all phonon modes and over the phonon spectrum. A numerical value was obtained by calculating the equations given by Mushgrave<sup>27</sup> on  $8 \times 256$  points in  $k$  space. By using these parameters a value  $f\lambda = 0.27 \text{ cm}^{-1}$  is calculated from the more reliable of the two values of  $T_2 T$ , namely, that determined from the linewidth results.

The agreement within a factor of 2 with the very rough estimates of 0.09 and 0.11  $\text{cm}^{-1}$  determined from the interpretation of the static spectrum must

TABLE III. Summary of important parameters for  $\text{CaF}_2:\text{O}^-$ .

$\lambda = 180 \text{ cm}^{-1}$ —unquenched spin-orbit coupling, from Ref. 25;
$E_{\text{JT}} = 970 \text{ cm}^{-1}$ —Jahn-Teller energy (see Fig. 2) as deduced from Eq. (2);
$\alpha = 1.8 \text{ cm}^{-1}$ —halfwidth of the distribution of strain interaction energies $V_B \epsilon_\alpha$ and $V_B \epsilon_\beta$ as determined from Eq. (3) and Fig. 4;
$V_B = 4.1 \times 10^{-12} \text{ erg/unit strain}$ —strain-coupling coefficient, from the slope of Fig. 3, using $\ln(N_1/N_2) = 3V_B(S_{11} - S_{12})P/2kT$ , and the compliance coefficients from Ref. 26;
$T_2T = 1.2 \times 10^{-7} \text{ sec}^\circ\text{K}$ —relaxation-time-temperature product deduced from linewidth analysis;
$T_2T = 2.1 \times 10^{-7} \text{ sec}^\circ\text{K}$ —deduced from microwave saturation of the ESR;
$\sum_\mu \langle G_\mu^{4k}/S_\mu^5 \rangle = 2.4 \times 10^{-29} \text{ sec}^5/\text{cm}^5$ —average inverse fifth power of the velocity of sound calculated using Ref. 27;
$f\lambda = 0.09 \text{ cm}^{-1}$ —reduced spin-orbit coupling, from stress-induced enhancement of the static spectrum;
$f\lambda = 0.11 \text{ cm}^{-1}$ —from linewidth as a function of applied stress;
$f\lambda = 0.27 \text{ cm}^{-1}$ —from reorientation theory and linewidth vs $T$ ;
$f\lambda = 0.20 \text{ cm}^{-1}$ —from reorientation theory and saturation measurements;
$f = 0.9 \pm 0.5 \times 10^{-3}$ —Jahn-Teller reduction factor from $\lambda$ and $f\lambda$ ;
$\hbar\omega = 210 \pm 15 \text{ cm}^{-1}$ —effective $E$ -mode vibrational frequency using $f$ , $E_{\text{JT}}$ , and the relation $f = e^{(-3E_{\text{JT}}/2\hbar\omega)}$ .

be considered satisfactory in view of the crudity of analysis of the static problem. In contrast with most systems in which the phonon-assisted tunnel-

ing is assumed the dominant reorientation mechanism, in this example one has an independent measure of the tunneling matrix element,  $f\lambda$  for this problem, and this comparison of  $f\lambda$  determined in two different ways becomes a quantitative test of the ideas of Sussman,<sup>20,21</sup> a test which is successfully passed.

Finally, a further consistency check on the model is to use the Jahn-Teller energy as estimated from Eq. (2) and the experimentally determined reduction factor  $f$  to calculate an effective vibrational frequency for the Jahn-Teller  $E$  mode from the Ham prediction  $f = \exp(-3E_{\text{JT}}/2\hbar\omega)$ . The value of  $\hbar\omega$  so calculated is  $210 \text{ cm}^{-1}$ , certainly a reasonable value for the  $\text{CaF}_2$  host crystal.

## VI. CONCLUSION

The main conclusion of this investigation is that a dynamical Jahn-Teller model, as outlined schematically by Table III, satisfactorily accounts for most of the experimental features of the  $\text{O}^-$  center in  $\text{CaF}_2$ . The dominant reorientation process has been shown to be a phonon-assisted "tunneling" process in which the "tunneling" matrix element is the electronic spin-orbit coupling reduced by the Jahn-Teller interaction. The rough quantitative accord between the spin-orbit parameter deduced from the behavior of the static spectrum with applied stress and that deduced from the reorientation rate is, to our knowledge, the first quantitative confirmation, in the sense of there being no free parameters, of the theory of the phonon-assisted tunneling process. Finally we should note that there is a remarkable  $T^2$  temperature dependence of the  $g$  values for the  $\text{O}^-$  center in the regime  $T < 20^\circ\text{K}$  which does not seem to be explicable in terms of our idealization of this system.

## ACKNOWLEDGMENTS

One of the authors (H. B.) would like to thank Cornell University for its hospitality. He is further indebted to the University of Geneva and the Swiss National Science Foundation for financial support.

<sup>†</sup>This work has been supported by the U. S. Atomic Energy Commission under Contract No. AT(11-1)3150, Technical Report No. C00-3150-23. Additional support was received from the National Science Foundation under Grant No. GH-33637 through the Cornell Materials Science Center, Report No. 2211.

<sup>1</sup>M. D. Sturge, in *Solid State Physics*, edited by F. Seitz, D. Turnbull, and H. Ehrenreich (Academic, New York, 1967), Vol. 20, p. 91.

<sup>2</sup>F. S. Ham, in *Electron Paramagnetic Resonance*, edited by S. Geschwind (Plenum, New York, 1972).

<sup>3</sup>B. Bleaney, E. Ingram, Proc. Phys. Soc. Lond. A **63**, 408 (1950).

<sup>4</sup>R. H. Silsbee, Phys. Rev. **138**, A180 (1965).

<sup>5</sup>K. A. Müller, in *Magnetic Resonance and Relaxation*, edited by R. Blinc (North-Holland, Amsterdam, 1967), Vol. 14, p. 192.

<sup>6</sup>U. T. Hschli, Phys. Rev. **162**, 262 (1967).

<sup>7</sup>J. R. Herrington and T. L. Estle, Phys. Rev. B **3**, 2933 (1971).

<sup>8</sup>F. S. Ham, Phys. Rev. **138**, A 1727 (1965).

<sup>9</sup>G. W. Ludwig and H. H. Woodbury, in *Solid State Physics*, edited by F. Seitz and D. Turnbull (Academic, New York, 1962), Vol. 13, p. 223.

<sup>10</sup>H. Bill, R. Lacroix, Phys. Lett. **21**, 257 (1966).

<sup>11</sup>British Drug House, Dorset, England.

- <sup>12</sup>H. Bill, *Helv. Phys. Acta* 42, 771 (1969).  
<sup>13</sup>W. Bontinck, *Physica* 24, 650 (1958).  
<sup>14</sup>T. A. Castner, *Phys. Kondens. Mater.* 12, 104 (1970).  
<sup>15</sup>H. Bill, *Solid State Commun.* 9, 477 (1971).  
<sup>16</sup>W. Känzig, *J. Phys. Chem. Solids* 23, 479 (1962).  
<sup>17</sup>J. H. Van Vleck, *J. Chem. Phys.* 7, 72 (1939).  
<sup>18</sup>W. Moffitt, W. Thorson, *Phys. Rev.* 108, 1251 (1957).  
<sup>19</sup>A. M. Stoneham, *Rev. Mod. Phys.* 41, 82 (1969).  
<sup>20</sup>J. A. Sussman, *Phys. Kondens. Mater.* 2, 146 (1964);  
*J. Phys. Chem. Solids* 28, 1643 (1968).  
<sup>21</sup>R. Pirc, B. Zeks, P. Gosar, *J. Phys. Chem. Sol.* 27,  
1219 (1966).  
<sup>22</sup>P. W. Anderson, *J. Phys. Soc. Jap.* 3, 316 (1954).  
<sup>23</sup>D. W. Posener, *Aust. J. Phys.* 12, 184 (1959).  
<sup>24</sup>T. G. Castner, Jr., *Phys. Rev.* 130, 58 (1963).  
<sup>25</sup>H. R. Zeller, W. Känzig, *Helv. Phys. Acta* 40, 845  
(1967).  
<sup>26</sup>D. R. Huffmann, M. H. Norwood, *Phys. Rev.* 117, 709  
(1959).  
<sup>27</sup>M. J. P. Mushgrave, *Proc. R. Soc. Lond.* A226, 339  
(1954).